



OPEN ACCESS

EDITED BY

Long Fan,
University of Alaska Fairbanks,
United States

REVIEWED BY

Kun Zhang,
Henan Polytechnic University, China
Xingzong Liu,
Ludong University, China
Yu Zhang,
Tsinghua University, China

*CORRESPONDENCE

Donglin Dong,
ddl@cumtb.edu.cn
Zilong Guan,
2017029007@chd.edu.cn

SPECIALTY SECTION

This article was submitted to Economic
Geology,
a section of the journal
Frontiers in Earth Science

RECEIVED 30 October 2022

ACCEPTED 21 November 2022

PUBLISHED 20 January 2023

CITATION

Tang F, Dong D, Xiao Z and Guan Z
(2023), Analysis of failure characteristics
of grouting concretion body under the
action of water-force coupling.
Front. Earth Sci. 10:1084117.
doi: 10.3389/feart.2022.1084117

COPYRIGHT

© 2023 Tang, Dong, Xiao and Guan. This
is an open-access article distributed
under the terms of the [Creative
Commons Attribution License \(CC BY\)](https://creativecommons.org/licenses/by/4.0/).
The use, distribution or reproduction in
other forums is permitted, provided the
original author(s) and the copyright
owner(s) are credited and that the
original publication in this journal is
cited, in accordance with accepted
academic practice. No use, distribution
or reproduction is permitted which does
not comply with these terms.

Analysis of failure characteristics of grouting concretion body under the action of water-force coupling

Fei Tang¹, Donglin Dong^{1*}, Zhen Xiao² and Zilong Guan^{3*}

¹Department of Geological Engineering and Environment, China University of Mining and Technology, Beijing (CUMTB), Beijing, China, ²Hebei Geological Environment Monitoring Institute, Shijiazhuang, China, ³Institute of Ecological and Environmental Engineering, Power China Northwest Engineering Corporation Limited, Xi'an, China

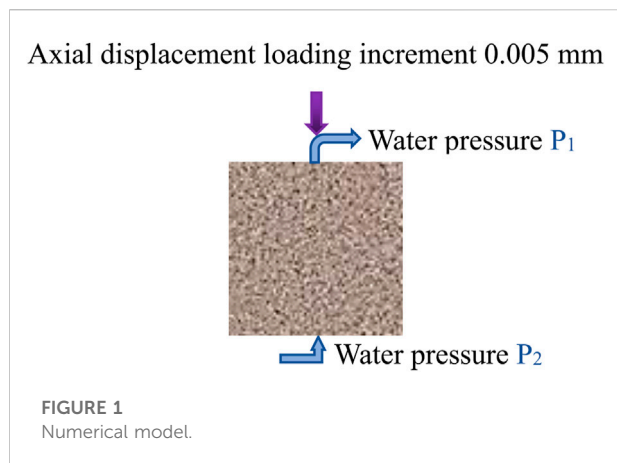
Cement slurry is widely used in grouting reinforcement of coal mine floor. Under the action of water-force coupling, the floor of abandoned roadway reinforced by cement slurry is prone to damage. The failure characteristics of grouting concretion body under water-force coupling were studied by using RFP software considering the heterogeneity of rock mass. The numerical simulation results show that the acoustic emission (AE) of numerical samples of the same strength with different lower boundary pressure decreases with the increase of lower boundary pressure, and the acoustic emission of numerical samples of the same lower boundary pressure with different strength increases with the increase of compressive strength. The lower the water pressure at the lower boundary is, the lower the softening degree of the sample is, and the sample is more prone to brittle fracture under external load. The numerical simulation results have important guiding significance for the grouting concretion body protection of coal mine floor in the future.

KEYWORDS

rock mechanics, water-force coupling, stress, acoustic emission, numerical simulation

Introduction

Due to the long geological evolution process and chamber excavation, the supporting pressure of surrounding rock exceeds its peak strength, and there must be a large number of weak planes (such as joints, fractures) in the rock mass (Hyett et al., 1992; Nikbakhtan and Osanloo, 2009; Xiujun et al., 2012). In underground engineering construction, grouting method is often used to strengthen and control, so as to improve the bearing capacity and waterproof performance of surrounding rock and ensure the safety of engineering construction (Tuerkmen and Oezguez, 2003; He et al., 2005; Zhang et al., 2015a). When the coal mining face is completed, the floor of the abandoned roadway will receive the action of external force and water pressure. Under the action of water-force coupling, grouting concretion body in coal mine floor is prone to cracking and crushing (Meng et al., 2013; Xie et al., 2015).

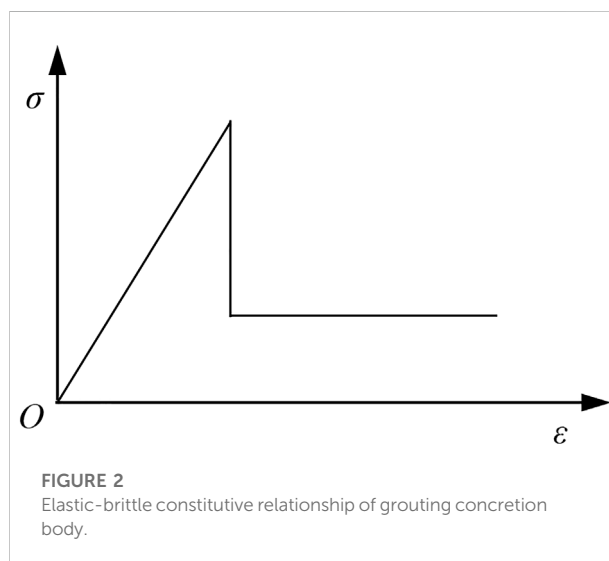


The stability control of weak and broken surrounding rock has always been one of the major problems puzzling the safety and efficient production of coal mines (Zhao et al., 2017; Liu et al., 2018; Wang et al., 2018; Wang et al., 2019; Zhou et al., 2020). Under the influence of high stress, fault fracture zone and weak cementation, the broken degree of surrounding rock is high, and the phenomena of roof fall and floor heave occur frequently (Gao et al., 2004; Pan et al., 2020). The strength and frequency of roadway repair are increased, and grouting reinforcement can improve self-bearing capacity of surrounding rock *in situ*. Grouting reinforcement technology is an efficient roadway support method in the process of coal mining, it is mainly through the injection of a certain slurry material into the surrounding rock to effectively support the roadway. However, groundwater can affect the strength of the grouting concretion body, and even cause roadway damage (Zhang et al., 2015b; Niu et al., 2017; Fan and Ma, 2018; Cai, 2020).

As early as the 1980s, P. D. Evdokimov et al. studied the influence of grouting on shear properties of fractured rock mass (Evdokimov et al., 1970). In the 1990s, Zhou et al. (1993) strengthened and grouted the weakly weathered rock mass near the base surface during the construction of Ertan Arch Dam, and theoretically analyzed the mechanism of rock mass mechanical changes by fracture-damage mechanics method. Zong et al. (2013) carried out the confined grouting reinforcement of cracked rock samples and tested the mechanical properties of grouting reinforced samples by using self-made grouting system. Han et al. (2011) revealed the essence and mechanisms of grouting reinforcement, measured the roughness of structural plane in cracked rock mass, and analyzed the influence of grouting on strength, joint roughness coefficient and stiffness of structural plane through the shear test of structural plane of rupture rock sample around grouting reinforcement. Wang et al. (2007) carried out experimental research on the mechanical properties of post-peak grouting reinforcement samples, and found that the higher the strength of the reinforced solid itself, the higher the strength of the grouting reinforced solid, and the higher

TABLE 1 Physical and mechanical parameters of grouting concretion body.

Parameter	Grouting concretion body
Homogeneity index	3
Young's modulus (GPa)	5.08
Poisson's ratio	0.2
Density (kg/m ³)	2,450
Friction angle (°)	45



the bond strength of the slurry, the higher the strength after grouting. Lei et al. (2015) defined the material parameters of irregular concretion, and analyzed the characteristics of stress and deformation under loads after grouting. Wael et al. (2021) discussed the influence of five different sizes of sand on the ultimate stress (MPa) of hand-mixed cement-grouted sands modified with polymer. Liu et al. (2021) analyzed influences on the performance of cement-based grout used to reform the upper Middle Ordovician limestone in Hanxing mining area. Zhang and Barry (2019) used the finite element method to examine the relative influence of a number of key factors controlling the stability and surface deformations of shallow, horizontal coal mine goafs overlain by sedimentary rock and grouting concretion body. Zhang et al. (2019) compared the microscopic properties of a new borehole sealing material with ordinary cement grout. From the above analysis, it can see that the effect of different water pressures on the fracture characteristics of grouting concretion body has not been studied.

In 1995, Professor Tang proposed the real failure process analysis method, namely the RFPA (Realistic Failure Process Analysis) method (Chen et al., 2021a). This method is based on the basic theory of finite element and fully considers the

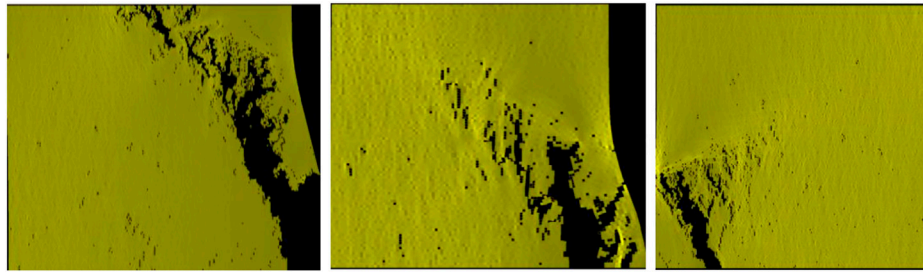


FIGURE 3
Failure modes of water pressure samples with the same strength and different lower boundaries.

characteristics of non-linearity, inhomogeneity and anisotropy that accompany the rock fracture process (Tang et al., 2000; Tang, 2003; Chen et al., 2021b). RFPA is a real fracture process analysis system that uses elastic mechanics as a stress analysis tool and elastic damage theory as a medium deformation analysis module (Chen et al., 2022; Yang, 2004).

In this paper, based on the above research, the failure characteristics of grouting concretion body under water-force coupling are studied by using RFPA software considering the heterogeneity characteristics of rock mass.

Introduction to RFPA-Flow

A brief introduction to the basic principles of RFPA-Flow

- 1) The seepage process in the rock satisfies the Biot consolidation theory (Tang, 2003; Yang, 2004).

$$\text{Equilibrium equation: } \frac{\partial \sigma_{ij}}{\partial x_{ij}} + \rho X_j = 0 \quad (i, j = 1, 2, 3) \quad (1)$$

$$\text{Geometric equation: } \varepsilon_{ij} \frac{1}{2} (u_{i,j} + u_{i,j}) \varepsilon_v = \varepsilon_{11} + \varepsilon_{22} + \varepsilon_{33} \quad (2)$$

$$\text{Constitutive equation: } \sigma_{ij} = \sigma_{ij} - \alpha p \delta_{ij} = \lambda \sigma_{ij} \varepsilon_v + 2G \varepsilon_{ij} \quad (3)$$

$$\text{Seepage equation: } K \nabla^2 p = \frac{1}{Q} \frac{\partial p}{\partial t} - \alpha \frac{\partial \varepsilon_v}{\partial t} \quad (4)$$

where ρ is the density, σ_{ij} is the stress tensor, ε_v is the volume strain, δ is the Kronecker constant, G is the shear modulus, λ is the Lamé coefficient, ∇^2 is the Laplace operator.

- 2) The relationship between permeability and stress-strain function is satisfied in the elastic state of microscopic unit, and the permeability K_f increases after the element is damaged and ruptured, the K_f can be written as:

$$K_f = K_0 e^{-b'} \quad (5)$$

- 3) The rock structure is non-uniform, and the damage parameters of the unit bodies composing the rock satisfy a certain probability distribution.

Element permeability-damage coupling equation

When the stress state of the meso-element meets a given damage threshold, the element begins to be damaged, and the elastic modulus of the damaged element is:

$$E = (1 - D)E_0 \quad (6)$$

where D is the damage variable, E and E_0 are the elastic modulus of damaged and undamaged elements respectively.

For the element subjected to uniaxial compression, the failure criterion of the element adopts the Mohr-Coulomb criterion, namely:

$$F = \sigma_1 - \sigma_3 \frac{1 + \sin \phi}{1 - \sin \phi} \geq f_c \quad (7)$$

where ϕ is the internal friction angle; f_c is the uniaxial compressive strength.

When the shear stress reaches the Mohr-Coulomb damage threshold, the damage variable D is expressed as follows:

$$D = \begin{cases} 0 & \varepsilon < \varepsilon_{c0} \\ 1 - \frac{f_{cr}}{E_0 \varepsilon} & \varepsilon_{c0} < \varepsilon \end{cases} \quad (8)$$

where f_{cr} is the uniaxial compressive residual strength, ε_{c0} is the maximum compressive strain, ε is the residual strain. It can be seen from the test that the damage will cause the permeability coefficient of the rock mass to increase sharply, and the change of the unit permeability coefficient can be described by the following formula:

$$\lambda = \begin{cases} \lambda_0 \partial^{-\beta} (\sigma_1 - \partial p) & D = 0 \\ \xi \lambda_0 \partial^{-\beta} (\sigma_1 - \partial p) & D > 0 \end{cases} \quad (9)$$

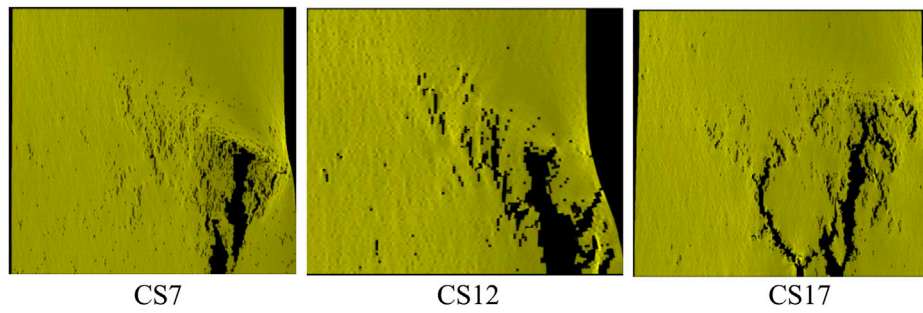


FIGURE 4
Failure modes of samples with different strength under water pressure at the same lower boundary.

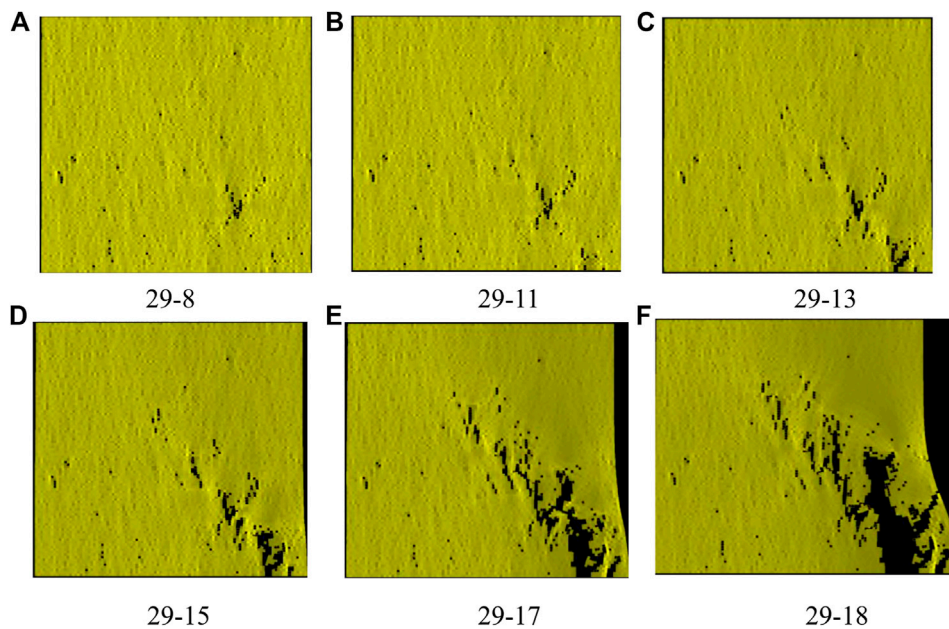


FIGURE 5
Fracture process of WP5 (CS5) sample. Loading step 29-8, Loading step 29-11, Loading step 29-13, Loading step 29-15, Loading step 29-17, Loading step 29-18.

where λ_0 is the initial permeability coefficient, p is the pore pressure, ξ , ∂ , β are the increase rate of the permeability coefficient, the pore pressure coefficient and the coupling coefficient, respectively.

Numerical model

The size of the grouting concretion body is 70.7 mm \times 70.7 mm, and the numerical model is composed of 202 \times 202 mesoscopic units. The mechanical parameters of the unit obey the Weibull distribution. The mechanical model of the

grouting concretion body under the action of water-force coupling is simplified into a plane strain problem in RFPA software for research (see Figure 1). The physical and mechanical parameters of grouting concretion body are shown in Table 1. The displacement loading method is adopted, and the displacement increment of each step is 0.005 mm/step. As the grouting concretion body belongs to brittle material, which is compressive but not tensile, the constitutive relationship of grouting concretion body in numerical simulation is simplified to elastic brittleness, as shown in Figure 2.

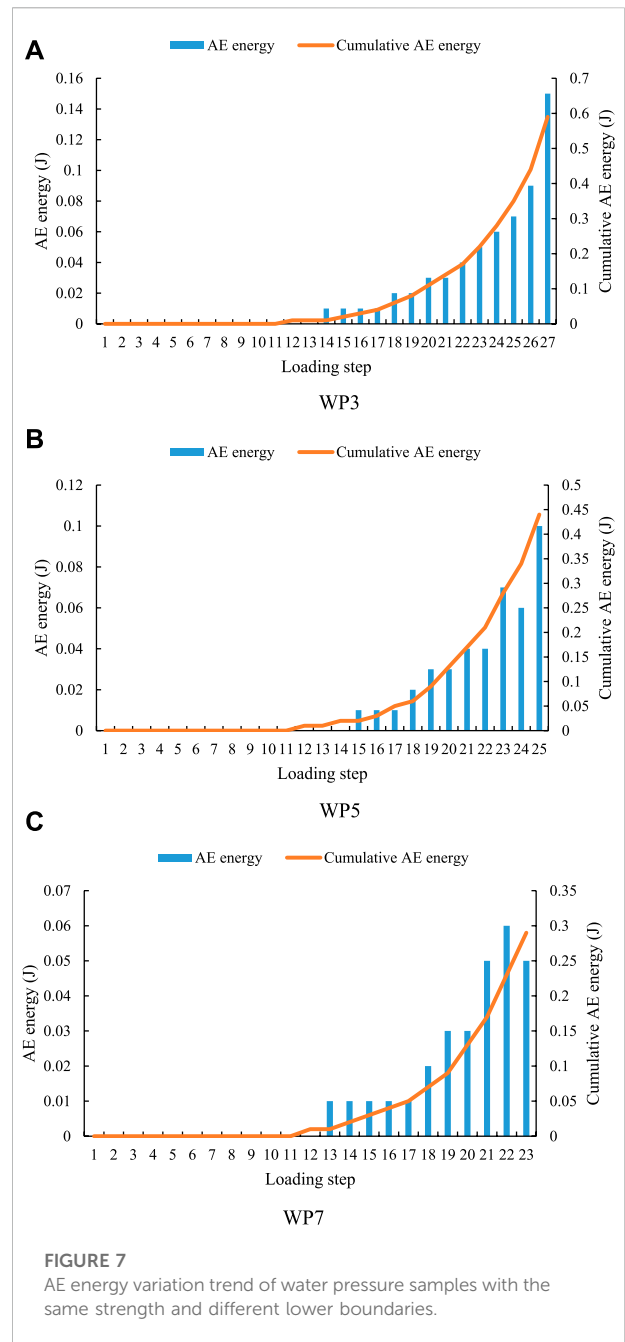
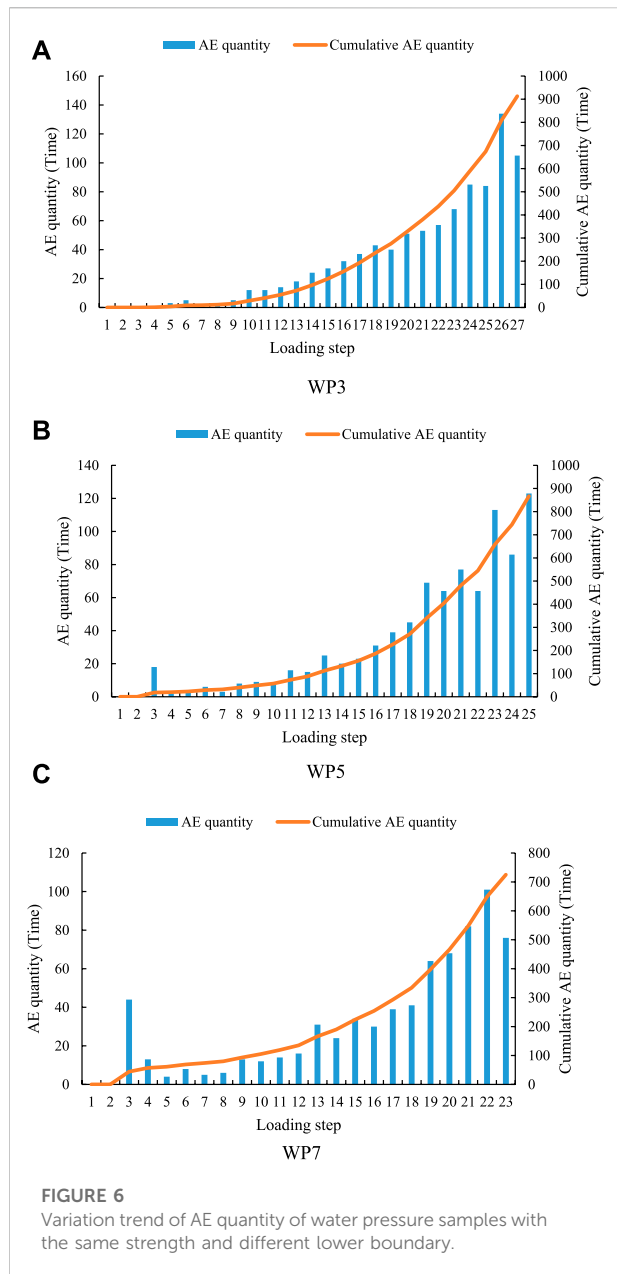
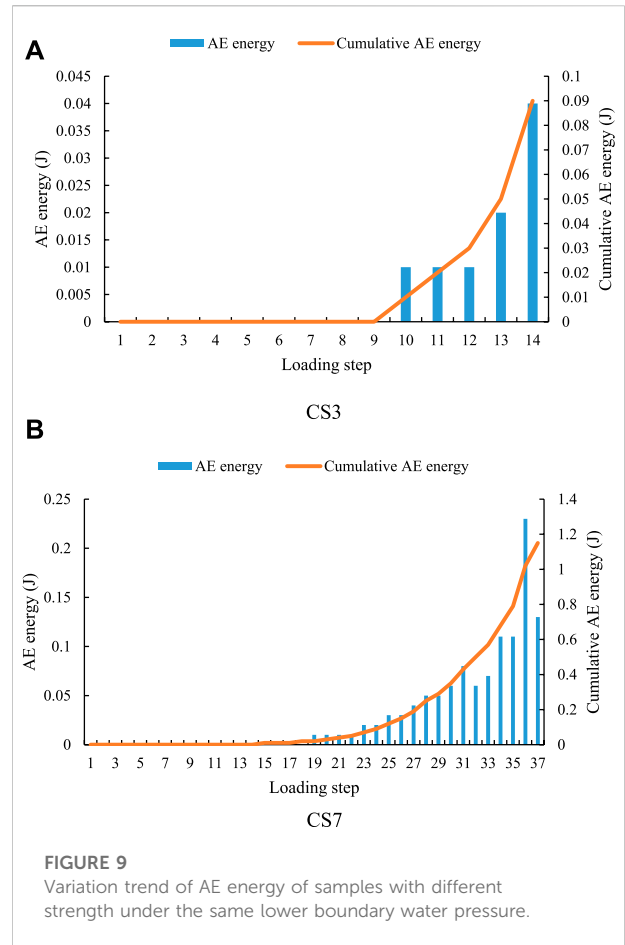
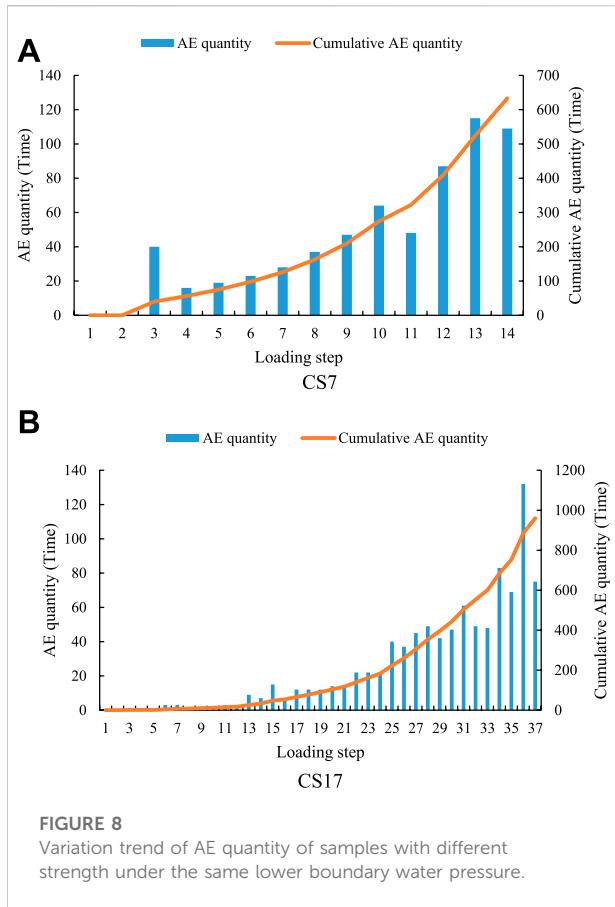


TABLE 2 AE values of different lower boundaries water pressure samples with the same strength.

Numerical model	WP3	WP5	WP7
Maximum AE quantity (Time)	134	123	101
Cumulative AE quantity (Time)	913	867	725
Maximum AE energy(J)	0.15	0.1	0.06
Cumulative AE energy(J)	0.59	0.44	0.29

In order to study the influence of different water pressure on the failure characteristics of grouting concrete body, the compressive strength of grouting concrete body is 12.55 MPa, the upper boundary water pressure P_1 is 1 MPa, and the lower boundary water pressure P_2 is 3 MPa, 5 MPa and 7 MPa respectively. Each sample is marked as WP3, WP5 and WP7 respectively. In order to study the failure characteristics of grouting concrete bodies with



different compressive strengths under the action of water-force coupling, the upper boundary water pressure and the lower boundary water pressure of the numerical model are taken as 1 MPa and 5 MPa respectively, and the compressive strengths of the grouting concrete bodies are 7.55 MPa, 12.55 MPa and 17.55 MPa respectively. Each sample is marked as CS7, CS12 (WP5) and CS17 respectively. Note: In two different comparative tests, WP5 sample and CS12 sample are the same sample.

Numerical simulation results and analysis

Comparative analysis of specimen fracture morphology

Figure 3 shows the failure modes of water pressure samples with the same strength and different lower boundaries. It can be seen from Figure 3 that when the lower boundary water pressure is 3 MPa, the fracture morphology of the sample is the most serious, and a serious fracture zone appears on the right side of the sample. When the water pressure at the lower boundary is 7 MPa, the fracture morphology of the sample is relatively light,

and only a macroscopic crack appears in the lower left corner of the sample. When the water pressure at the lower boundary is 5 MPa, the fracture severity of the sample is between the lower boundary water pressure of 3 MPa and 7 MPa, and a serious fracture zone appears in the lower right corner of the sample. The above numerical test phenomenon shows that the smaller the lower boundary water pressure the specimen bears, the more serious the fracture morphology of the specimen. The reason for the above test phenomenon is that the lower the water pressure at the lower boundary is, the lower the softening degree of the sample is, and the sample is more prone to brittle fracture under external load. The greater the water pressure at the lower boundary, the higher the softening degree of the sample, and the sample is more likely to crack in a certain local area under the action of external load.

Figure 4 shows the failure modes of samples with different strength under water pressure at the same lower boundary. As can be seen from Figure 4, when the compressive strength of the sample is 17.55 MPa, the fracture morphology of the sample is the most serious, and multiple macroscopic penetrating fracture zones appear on the right side of the sample. When the compressive strength of the sample is 7.55 MPa, the fracture morphology of the sample is

TABLE 3 AE values of samples with different strength under the same lower boundary water pressure.

Numerical model	CS7	CS12 (WP5)	CS17
Maximum AE quantity (Time)	115	123	132
Cumulative AE quantity (Time)	633	867	960
Maximum AE energy(J)	0.04	0.1	0.23
Cumulative AE energy(J)	0.09	0.44	1.15

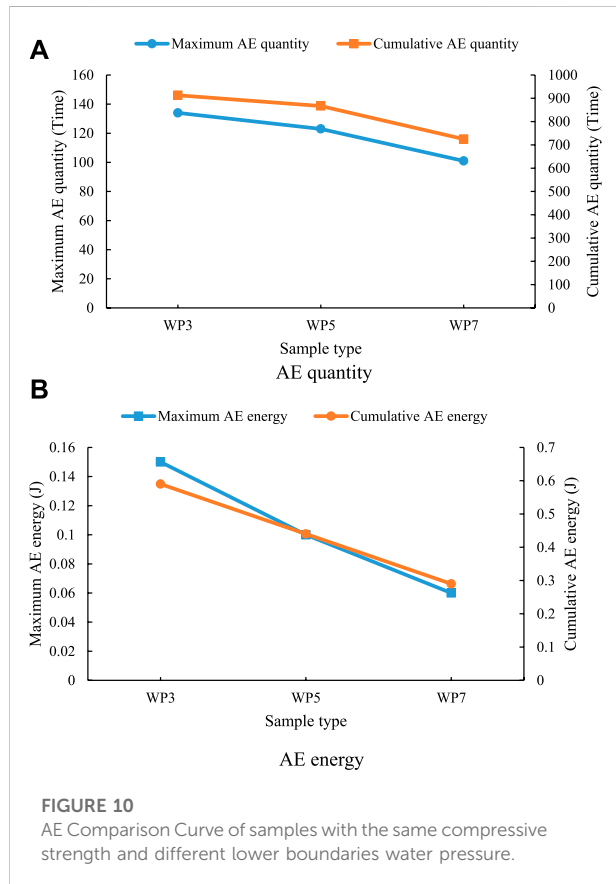


FIGURE 10 AE Comparison Curve of samples with the same compressive strength and different lower boundaries water pressure.

relatively light, and only a macroscopic crack appears in the lower right corner of the sample. When the compressive strength of the sample is 12.55 MPa, the fracture severity of the sample is between the compressive strength of 7.55 MPa and 17.55 MPa. A macroscopic crack also appears in the lower right corner of the sample, and there is a macroscopic penetrating crack in the upper left side of this macroscopic crack. The above numerical test phenomenon shows that the greater the compressive strength of the sample, the more serious the fracture morphology of the sample.

Figure 5 shows the fracture process of WP5 sample (with compressive strength of 12.55 MPa and lower boundary water pressure of 5 MPa). Under the influence of inhomogeneity, the unit with weak strength in the sample first breaks, as shown in

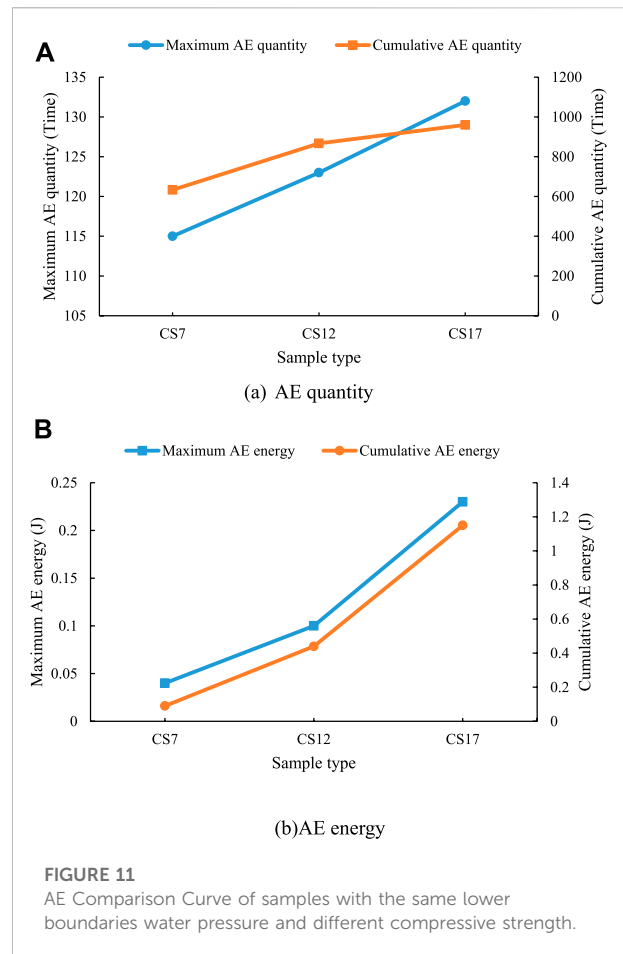
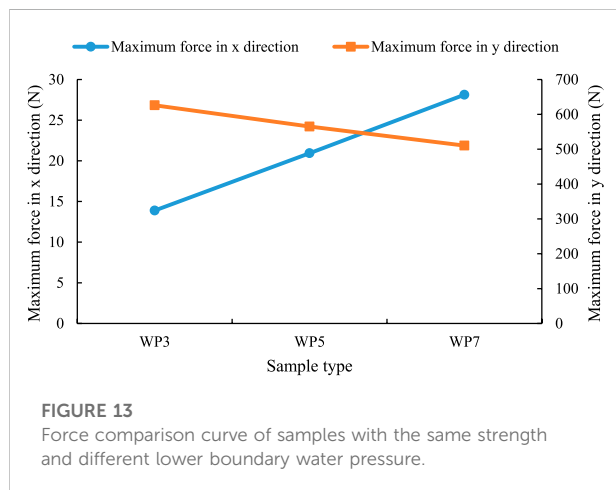
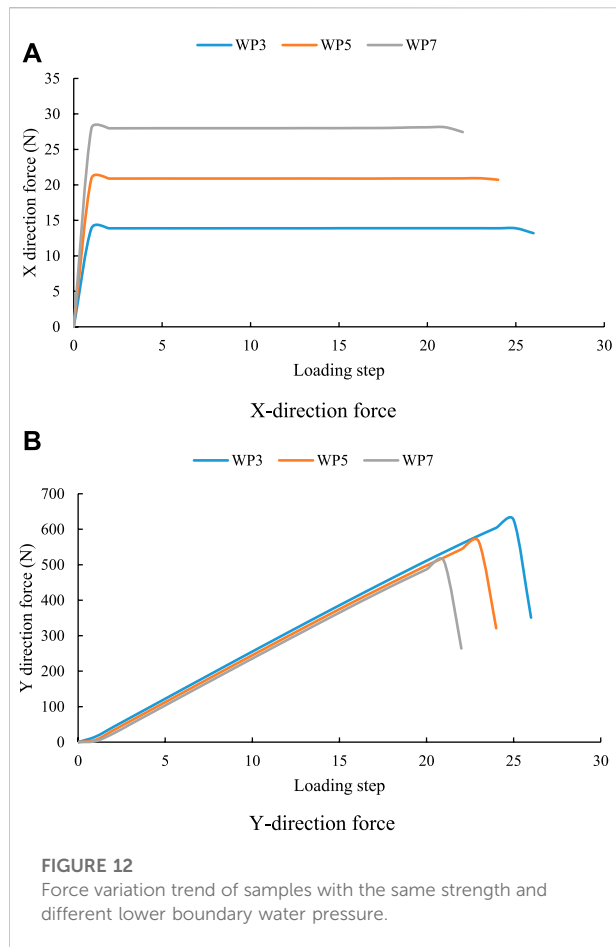


FIGURE 11 AE Comparison Curve of samples with the same lower boundaries water pressure and different compressive strength.

Figure 5A,B. Continue to load. Since the water pressure at the lower part of the sample is higher than that at the upper part, the lower part of the sample also breaks, as shown in Figure 5C. Under the combined action of external force and water pressure, the cracks inside the sample and the cracks at the lower boundary of the sample slowly penetrate, as shown in Figure 5D,E. When the external force further increases and exceeds the compressive strength of the rock mass, the crack already penetrated in the lower right corner of the sample further increases and finally forms a macroscopic crack, as shown in Figure 5F.

Comparative analysis of AE parameters

As shown in Figures 6, 7, when the water pressure at the lower boundary is 3 MPa, the AE quantity reaches the maximum of 134 at step 26 (see Table 2), and the AE energy reaches the maximum of 0.15 J at step 27. When the water pressure at the lower boundary is 5 MPa, the AE quantity and energy have two peaks. The AE quantity reached the maximum of 123 at step 25, and the AE energy also reached the maximum of 0.1 J at step 25. At the beginning of the force, the AE quantity shows a sudden rise and fall phenomenon at



the third step. Moreover, the quantity and energy of AE also appear the first peak at step 23. When the quantity and energy of AE reach the peak for the second time, the sample is completely destroyed. The appearance of the first peak can be used as an early warning, indicating that the sample is about to be completely destroyed.

TABLE 4 Maximum force of lower boundary water pressure samples with the same strength.

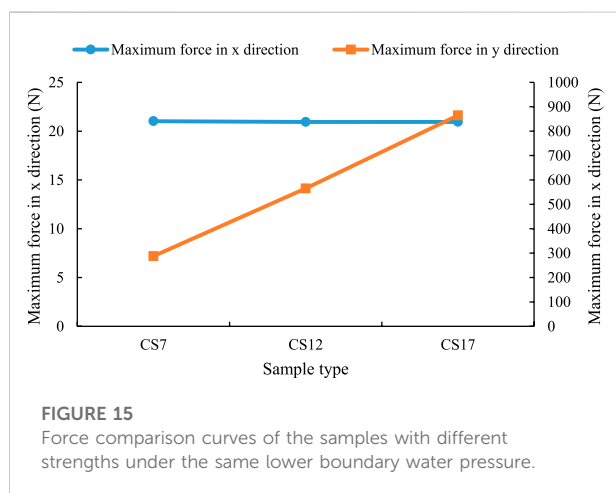
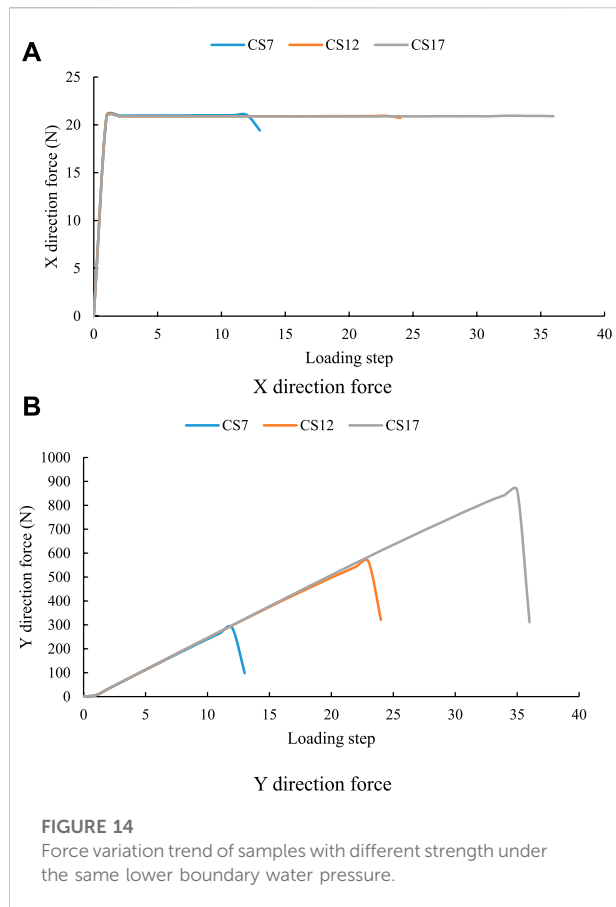
Numerical model	WP3	WP5	WP7
Maximum force in x direction (N)	13.89	20.94	28.13
Maximum force in y direction (N)	626.06	565.11	510.37

When the water pressure at the lower boundary is 7 MPa, the AE quantity reaches the maximum value of 101 at step 22, and the AE energy reaches the maximum value of 0.06 J at step 22. At the beginning of the force, the quantity of AE shows a sudden rise and fall phenomenon at the third step. No matter what kind of water pressure the sample is subjected to, the AE cumulative quantity curve and the AE cumulative energy curve are relatively smooth, and there is no obvious jump phenomenon. It can be seen from the above analysis that with the increase of water pressure at the lower boundary, the times when the maximum value of AE quantity and energy occurs are earlier.

As shown in Figures 8, 9, when the compressive strength of the sample is 7.55 MPa, the AE quantity of the sample reaches the maximum of 115 at step 13 (see Table 3), and the AE quantity shows a sudden rise and fall phenomenon at step 3. The AE energy of the sample appears in step 10. Continue loading, and the AE energy reaches the maximum value of 0.04 J in step 14. When the compressive strength of the sample is 17.55 MPa, the AE quantity of the sample reaches the maximum of 132 in step 36, and the AE energy also reaches the maximum of 0.23 J in step 36. Since CS12 and WP5 are the same sample, the variation trend of AE quantity and energy of CS12 sample is shown in sample WP5. It can be seen from the above analysis that with the increase of the compressive strength of the sample, the time when the maximum value of AE quantity and energy occurs is later. This experimental phenomenon shows that the greater the compressive strength of the sample, the stronger the failure resistance of the sample. Under the same external conditions, increasing the water cement ratio of the sample can improve the service time of the sample.

As shown in Figure 10, when the water pressure at the lower boundary is 3 MPa, the maximum AE quantity, cumulative AE quantity, maximum AE energy, and cumulative AE energy are all the largest. When the water pressure at the lower boundary is 7 MPa, the maximum AE quantity, cumulative AE quantity, maximum AE energy and cumulative AE energy are all the minimum. This numerical simulation phenomenon shows that the AE decreases gradually with the increase of the water pressure at the lower boundary. Moreover, the maximum AE energy and the accumulated AE energy obviously decrease linearly.

As shown in Figure 11, when the compressive strength is 7.55 MPa, the maximum AE quantity, cumulative AE quantity, maximum AE energy, and cumulative AE energy are all minimum. When the water pressure at the lower boundary is 17.55 MPa, the



maximum AE quantity, the cumulative AE quantity, the maximum AE energy and the cumulative AE energy are all the largest. This numerical simulation phenomenon shows that the AE increases gradually with the increase of compressive strength. Moreover, the maximum AE energy and the accumulated AE energy show a significant increase.

TABLE 5 Maximum force values of samples with different strength under the same lower boundary water pressure.

Numerical model	CS7	CS12 (WP5)	CS17
Maximum force in x direction (N)	21.02	20.94	20.95
Maximum force in y direction (N)	287.59	565.11	864.54

Comparative analysis of force

The force curves in the X direction of the three samples with the same compressive strength and different lower boundary water pressure basically do not change with the increase of external force, and the slope of the force curves in the Y direction of the growth stage is basically the same (see Figure 12). The maximum forces on the X direction of the three samples from large to small are WP3, WP5 and WP7 (see Figure 13), and their values are 13.89 N, 20.94 N and 28.13 N respectively (see Table 4). The maximum forces on the Y direction of the three samples from large to small are WP7, WP5 and WP3, and their values are 626.06 N, 565.11 N and 510.37 N respectively. Regardless of the water pressure at the lower boundary, the force in the Y direction is far greater than that in the X direction. The maximum force in X direction increases linearly with the increase of water pressure, while the maximum force in Y direction decreases linearly with the increase of water pressure.

The force curve in the X direction of the three samples with the same compressive strength and different lower boundary water pressure basically does not change with the increase of external force, and the slope of the force curve in the Y direction of the growth stage is basically the same (see Figure 14). The maximum forces in the X direction of the three samples are basically the same (see Figure 15), and their values are 21.02 N, 20.94 N and 20.95 N respectively (see Table 5). The maximum force values of the three samples in Y direction from small to large are CS7, CS12 and CS17, whose values are 287.59 N, 565.11 N and 864.54 N, respectively. Regardless of the compressive strength of the sample, the force in Y direction is much larger than that in X direction. The maximum force in the X direction has no obvious relationship with the compressive strength of the sample, while the maximum force in the Y direction increases linearly with the increase of compressive strength, and the increase amplitude is very large.

Conclusion

Different lower boundary water pressure and different compressive strength lead to different fracture forms of the samples. However, the force curves in the X direction all show elastic-plastic, and the force curves in the Y direction all show elastic-

brittle. The greater the lower boundary water pressure is, the higher the softening degree of the sample is, and the sample is more likely to crack in a certain local area under the action of external load.

Under the same external conditions, increasing the compressive strength of the sample, that is, increasing the water-cement ratio of the sample, can improve the service life of the sample. However, the brittleness of the samples increases with the increase of the compressive strength, and the brittle fracture morphology of the samples becomes more serious.

The AE values and the maximum force in X direction of the samples with different lower boundary water pressure of the same compressive strength decrease inversely with the lower boundary water pressure. The maximum force in Y direction increases in direct proportion to the lower boundary water pressure.

The AE quantity and the maximum force in Y direction of the samples with different strength under the same lower boundary water pressure increase in positive proportion to the compressive strength of the samples. The maximum force in X direction has no correlation with the compressive strength of the sample, and the maximum force in X direction of the three samples is basically the same.

Data availability statement

The original contributions presented in the study are included in the article/supplementary material, further inquiries can be directed to the corresponding authors.

References

- Cai, M. F. (2020). Key theories and technologies for surrounding rock stability and ground control in deep mining[J]. *J. Min. Strata Control Eng.* 2 (3), 5–13. doi:10.13532/j.jmsce.cn10-1638/td.20200506.001
- Chen, F., Du, Y-H., Sun, X-M., Ma, T-H., and Tang, C. (2021). Numerical experimental study on influence factors of anchoring force of constant resistance bolt. *Geomat. Nat. Hazards Risk* 12 (1), 424–442. doi:10.1080/19475705.2021.1880490
- Chen, F., Wang, X-B., Du, Y-H., and Tang, C. (2021). Numerical analysis of the precursory information of slope instability process with constant resistance bolt. *Sci. Rep.* 11 (1), 21814–21910. doi:10.1038/s41598-021-01387-z
- Chen, F., Wang, X-B., Du, Y-H., and Tang, C. (2022). Numerical experiment research on failure characteristics of anchored rock with negative Poisson's ratio bolt[J]. *Front. Earth Sci.* 10, 1–10. doi:10.3389/feart.2022.89975
- Evdokimov, P. D., Adamovich, A. N., Fradkin, L. P., and Denisov, V. N. (1970). Shear strengths of fissures in ledge rock before and after grouting. *Hydrotech. Constr.* 4 (3), 229–233. doi:10.1007/bf02376472
- Fan, L., and Ma, X. (2018). A review on investigation of water-preserved coal mining in Western China. *Int. J. Coal Sci. Technol.* 5 (4), 411–416. doi:10.1007/s40789-018-0223-4
- Gao, Y., Fan, Q. Z., and Wang, H. (2004). Grouting reinforcement test of rock after peak value of strength and roadway stability control[J]. *Rock Soil Mech.* 25 (1), 21–24. doi:10.16285/j.rsm.2004.s1.005
- Han, L., Zong, Y., and Han, G. (2011). Study of shear properties of rock structural plane by grouting reinforcement[J]. *Rock Soil Mech.* 32 (9), 2570–2622. doi:10.16285/j.rsm.2011.09.011
- He, M., Xie, H., and Peng, S. (2005). Study on rock mechanics in deep mining engineering[J]. *Chin. J. Rock Mech. Eng.* 24 (16), 2803–2813
- Hyett, A. J., Ba Wden, W. F., and Reichert, R. D. (1992). The effect of rock mass confinement on the bond strength of fully grouted cable bolts. *Int. J. Rock Mech. Min. Sci. Geomechanics Abstr.* 29 (5), 503–524. doi:10.1016/0148-9062(92)92634-o
- Lei, J. S., Liu, F., and Wang, Q. F. (2015). Diffusion characteristics and reinforcement mechanics of grouting in non-homogeneous soil strata[J]. *Chin. J. Geotechnical Eng.* 32 (12), 2245–2253. doi:10.11779/CJGE201512014
- Liu, Q. S., Lei, G. F., Peng, X. X., Lu, C., and Wei, L. (2018). Rheological characteristics of cement grout and its effect on mechanical properties of a rock fracture. *Rock Mech. Rock Eng.* 51, 613–625. doi:10.1007/s00603-017-1340-x
- Liu, Z. X., Dong, S., and Wang, H. (2021). Influences on the performance of cement-based grout used to reform the upper Middle Ordovician limestone in Hanxing mining area[J]. *Arabian J. Geosciences* 14 (13), 1–15. doi:10.1007/s12517-021-07512-6
- Meng, B., Jing, H., Chen, K., and Su, H. (2013). Failure mechanism and stability control of a large section of very soft roadway surrounding rock shear slip. *Int. J. Min. Sci. Technol.* 23 (1), 127–134. doi:10.1016/j.ijmst.2013.03.002
- Nikbakhtan, B., and Osanloo, M. (2009). Effect of grout pressure and grout flow on soil physical and mechanical properties in jet grouting operations. *Int. J. Rock Mech. Min. Sci. (1997)*. 46 (3), 498–505. doi:10.1016/j.ijrmm.2008.10.005
- Niu, X., Wang, H., and Liu, S. (2017). Application and development trends on grouting reconstruction technology for floor karst aquifers of lower group coal seam in Northern China coal field[J]. *Mine Constr. Technol.* 38 (3), 24–30. doi:10.19458/j.cnki.cn11-2456/td.2017.03.008
- Pan, R., Cheng, H., and Wang, L. (2020). Experimental study on bearing characteristics of bolt grouting in shallow fractured surrounding rock of roadway[J]. *Rock Soil Mech.* 41 (6), 1887–1898. doi:10.16285/j.rsm.2019.6448

Author contributions

FT: Writing Original Draft and Data Curation; DD: Review; ZX: Conceptualization; ZG: Funding acquisition.

Funding

This study was supported by the National Natural Science Foundation of China (No. 41972255, 42207084).

Conflict of interest

The author ZG was employed by Power China Northwest Engineering Corporation Limited.

The remaining authors declare that the research was conducted in the absence of any commercial or financial relationships that could be construed as a potential conflict of interest.

Publisher's note

All claims expressed in this article are solely those of the authors and do not necessarily represent those of their affiliated organizations, or those of the publisher, the editors and the reviewers. Any product that may be evaluated in this article, or claim that may be made by its manufacturer, is not guaranteed or endorsed by the publisher.

- Tang, C. A. (2003). *Numerical experiments of rock failure process*[M]. Beijing: Science Press. (in Chinese).
- Tang, C. A., Liu, H., Lee, P. K. K., Tsui, Y., and Tham, L. G. (2000). Numerical studies of the influence of microstructure on rock failure in uniaxial compression - Part I: Effect of heterogeneity. *Int. J. Rock Mech. Min. Sci. (1997)* 37 (4), 555–569. doi:10.1016/s1365-1609(99)00121-5
- Tuerkmen, S., and Oezguez, N. (2003). Grouting a tunnel cave-in from the surface: A case study on kurtkula irrigation tunnel, Turkey[J]. *Tunn. Undergr. Space Technol. Incorporating Trenchless Technol. Res.* 18 (4), 365–375. doi:10.1016/S0886-7798(03)00007-5
- Wael, M., Ahmed Salih, M., and Parveen, S. (2021). Interpreting the experimental results of compressive strength of hand-mixed cement-grouted sands using various mathematical approaches[J]. *Archives Civ. Mech. Eng.* 22 (1), 1–25. doi:10.1007/s43452-021-00341-0
- Wang, H., Gao, Y., and Li, S. (2007). Uniaxial experiment study on mechanical properties of reinforced broken rocks pre-and-post grouting[J]. *Chin. J. Undergr. Space Eng.* 3 (1), 27–39.
- Wang, Q., Gao, H. K., Yu, H. C., Jiang, B., and Liu, B. (2019). Method for measuring rock mass characteristics and evaluating the grouting-reinforced effect based on digital drilling. *Rock Mech. Rock Eng.* 52, 841–851. doi:10.1007/s00603-018-1624-9
- Wang, Q., He, M. C., Yang, J., Gao, H., Jiang, B., and Yu, H. (2018). Study of a no-pillar mining technique with automatically formed gob-side entry retaining for longwall mining in coal mines. *Int. J. Rock Mech. Min. Sci.* 110, 1–8. doi:10.1016/j.ijrmms.2018.07.005
- Xie, H., Gao, F., and Yang, J. (2015). Research and development of rock mechanics in deep ground engineering[J]. *Chin. J. Rock Mech. Eng.* 34 (11), 2161–2178. doi:10.13722/j.cnki.jrme.2015.1369
- Xiujun, W., Gao, M., and Lv, Y. C. (2012). Evolution of a mining induced fracture network in the overburden strata of an inclined coal seam[J]. *Int. J. Min. Sci. Technol.* 22 (6), 775–779. doi:10.1016/j.ijmst.2012.11.004
- Yang, T. (2004). *Seepage characteristic in rock failure: Theory, model and application*[M]. Beijing: Science Press. (in Chinese).
- Zhang, C., Chang, J., and Li, S. (2019). Experimental study comparing the microscopic properties of a new borehole sealing material with ordinary cement grout[J]. *Environ. Earth Sci.* 78 (5), 1–11. doi:10.1007/s12665-019-8165-8
- Zhang, F., and Barry, L. (2019). A numerical study to assist assessment of the stability of shallow coal mine goafs. *Geotech. Geol. Eng. (Dordr.)* 37 (4), 2837–2846. doi:10.1007/s10706-018-00799-5
- Zhang, Q. S., Zhang, L. Z., and Liu, R. (2015b). Laboratory experimental study of cement-silicate slurry diffusion law of crack grouting with dynamic water[J]. *Rock Soil Mech.* 36 (8), 2159–2168. doi:10.16285/j.rsm.2015.08.005
- Zhang, R., Dai, F., Gao, M. Z., Xu, N., and Zhang, C. (2015a). Fractal analysis of acoustic emission during uniaxial and triaxial loading of rock. *Int. J. Rock Mech. Min. Sci. (1997). Min. Sci.* 79, 241–249. doi:10.1016/j.ijrmms.2015.08.020
- Zhao, K., Wang, H., and Xu, W. (2017). Experimental study on seepage characteristics of rock-like materials with consecutive and filling fractures[J]. *Chin. J. Geotechnical Eng.* 39 (6), 1130–1136. doi:10.11779/CJGE201706020
- Zhou, D., Zhao, Z., Bo, L., Chen, Y., and Ding, W. (2020). Permeability evolution of grout infilled fractures subjected to triaxial compression with low confining pressure. *Tunn. Undergr. Space Technol.* 104, 103539. doi:10.1016/j.tust.2020.103539
- Zhou, W., Yang, R., and Yan, G. (1993). Study on the efficacy of grouting reinforcement of slightly weathered rock masses at the Ertan arch dam abutments [J]. *Chin. J. Rock Mech. Eng.* 12 (2), 138–150.
- Zong, Y., Han, L., and Han, G. (2013). Mechanical characteristics of confined grouting reinforcement for cracked rock mass[J]. *J. Min. Saf. Eng.* 30 (4), 483–488.